CrossMark
click for updates

Mn₃O₄ hollow microcubes and solid nanospheres derived from a metal formate framework for electrochemical capacitor applications†

Zhihe Liu, Li Zhang,* Guancheng Xu, Lu Zhang, Dianzeng Jia* and Chuyang Zhang

Mn₃O₄ hollow microcubes and solid nanospheres were selectively fabricated from a metal formate framework ([CH₃NH₃][Mn(HCOO)₃]) by employing the ion exchange reaction in alkaline solution under different hydrothermal conditions. The relationships between Mn₃O₄ morphology and reaction molar ratio and reaction time were investigated. When used as the electrode materials for supercapacitors, Mn₃O₄ hollow microcubes and solid nanospheres had specific capacitances of 176 and 150 F g⁻¹ respectively at a current density of 0.3 A g⁻¹ in 1 M Na₂SO₄. The specific capacitance retentions of the Mn₃O₄ hollow microcubes and solid nanospheres were 95% and 86% respectively after 8000 charge–discharge cycles at a current density of 2 A g⁻¹. Electrochemical results show that the Mn₃O₄ hollow microcubes and solid nanospheres exhibit acceptable specific capacitance and excellent cycling stability.

Introduction

In recent years, dramatic increases of fossil fuel consumption and environmental pollution have already become severe challenges, so it is urgent to develop sustainable energy storage and conversion devices. Widely regarded as clean energy-storage devices, supercapacitors have attracted great attention due to their rapid charging and discharging, high power density and long-term cycling stability.[1–3] Generally, based on the energy storage mechanisms, there are two types of energy storage devices, *i.e.* electrical double layer capacitors (EDLCs) and pseudocapacitors.[4,5] EDLCs store energy through fast reversible adsorption and desorption of ions on the electrode and electrolyte interface,[6–9] and pseudocapacitors do so relying on fast redox reaction on the surface of electrode materials.[10,11] Electrode materials affect the performance of electrochemical capacitors.

Numerous electrode materials with high energy densities, such as NiO,[12] RuO₂,[13] Co₃O₄[14] and MnO₂,[15] have been developed. Among various transition metal oxides, manganese oxides are promising electrode materials, mainly due to large potential window, low cost and environmental friendliness.

However, the poor electrical/ionic conductivity and cycling stability of manganese oxides still limit their potential applications,[16] which has been overcome by fabricating materials with hollow microstructures. Such attractive structures not only provide more active faradaic sites but also facilitate the transport of electrons and electrolyte ions.

In addition, materials with hollow microstructures have been applied in Li-ion batteries and supercapacitors due to large surface area, low density, and tunable architecture. At present, hollow structures have generally been prepared by the template method. Various templates (carbon spheres,[17,18] polystyrene spheres,[19] cuprous oxide, *etc.*[20,21]) have been developed to synthesize different hollow metal oxides, involving tedious template preparation and removal procedures though. Therefore, it is desirable to develop a facile approach to prepare metal oxides with hollow structures.

Metal–organic frameworks (MOFs) have attracted much interest owing to large surface area and porosity, thus having become promising candidates for catalysis,[22,23] energy storage,[24] and gas separation.[25–28] Recently, MOFs have been used as novel templates to construct metals/metal oxides, carbon materials and metal oxide hybrids with well-defined morphologies under appropriate thermolysis conditions. For instance, Xu *et al.* fabricated porous α-Fe₂O₃ by annealing MIL-88-Fe.[29] Salunkhe *et al.* synthesized porous carbon and cobalt oxide through thermolysis of ZIF-67.[30] Zhang *et al.* synthesized Fe₂O₃ microboxes by annealing Fe₄[Fe(CN)₆]₃.[31] Moreover, some hollow metal oxides have been fabricated by alkaline-solution treatment of MOFs templates. For example, Zhang *et al.* prepared Fe₂O₃ hollow microboxes by alkaline-solution treatment of Fe₄[Fe(CN)₆]₃.[32] Zhang *et al.* synthesized Co₃O₄ hollow nanoboxes by reacting KCo[Fe(CN)₆]·3H₂O with NaOH solution.[33]

Key Laboratory of Energy Materials Chemistry (Xinjiang University), Ministry of Education, Key Laboratory of Advanced Functional Materials, Autonomous Region, Physics and Chemistry Detecting Center, Xinjiang University, Urumqi, 830046, Xinjiang, P. R. China. E-mail: zhanglixju@163.com; jdz0991@gmail.com; Fax: +86-991-8580586; Tel: +86-991-8580586

However, most synthetic procedures involve template calcination, so a facile approach is still in need to prepare hollow metal oxides.

In this study, we reported a facile strategy to prepare Mn_3O_4 hollow microcubes and solid nanospheres by employing the ion exchange reactions between a metal formate framework $[CH_3NH_3][Mn(HCOO)_3]$ and alkaline solution under different hydrothermal conditions. More importantly, when applied as supercapacitor electrode materials, Mn_3O_4 hollow microcubes and solid nanospheres had high specific capacitances of 176 F g^{-1} and 150 F g^{-1} respectively at a current density of 0.3 A g^{-1}. The specific capacitance retentions of Mn_3O_4 hollow microcubes and solid nanospheres were 95% and 86% respectively after 8000 charge–discharge cycles at a current density of 2 A g^{-1}.

Experimental

Chemicals

Manganese chloride ($MnCl_2 \cdot 4H_2O$, 99%), methylamine (30–33% in methanol), anhydrous formic acid (98.5%), polyvinylpyrrolidone K30 (PVP-K30), sodium hydroxide and ethanol were commercially available and used without further purification.

Synthesis of $[CH_3NH_3][Mn(HCOO)_3]$ microcube precursor

Cubic $[CH_3NH_3][Mn(HCOO)_3]$ precursor was synthesized as follows: CH_3NH_2 (5 mmol, 0.5171 g), HCOOH (5 mmol, 0.2301 g) and PVP-K30 (0.5 g) were dissolved in 25 mL of ethanol solution. Then 1 mmol $MnCl_2 \cdot 4H_2O$ (0.1979 g) and PVP-K30 (0.5 g) were dissolved in another 25 mL of ethanol, forming a homogeneous solution. Subsequently, the homogeneous solution was added dropwise into the former solution and reacted for 2 h. Finally, the white products were washed with ethanol several times and dried at 50 °C for 12 h.

Synthesis of Mn_3O_4 hollow microcubes

Mn_3O_4 hollow microcubes were obtained by reacting precursor $[CH_3NH_3][Mn(HCOO)_3]$ with NaOH in a molar ratio of 10 : 1. $[CH_3NH_3][Mn(HCOO)_3]$ (1 mmol, 0.2212 g) was dispersed into 50 mL of ethanol, and 0.1 mmol NaOH (0.004 g) was dissolved in 20 mL of ethanol and then added to the precursor solution with constant stirring. The mixture was transferred into a 100 mL autoclave and heated at 120 °C for 6 h. The final products were washed with deionized water and dried in an oven at 80 °C for 12 h.

Synthesis of Mn_3O_4 solid nanospheres

Mn_3O_4 solid nanospheres were obtained by reacting precursor $[CH_3NH_3][Mn(HCOO)_3]$ with NaOH in a molar ratio of 1 : 2. $[CH_3NH_3][Mn(HCOO)_3]$ (0.1 mmol, 0.0221 g) were dispersed in 50 mL of ethanol, and 0.2 mmol NaOH (0.008 g) was dissolved in 20 mL of ethanol and then added to precursor solution with constant stirring. The mixture was transferred into a 100 mL autoclave and heated at 120 °C for 24 h. The products were washed with deionized water and dried in an oven at 80 °C for 12 h.

Characterizations

Powder X-ray diffraction (XRD) was carried out to examine the phase of the samples using a Bruker D8 X-ray diffractometer equipped with Cu-Kα radiation ($\lambda = 1.5418$ Å) ranging from 10° to 80°. The morphologies and microstructures of the samples were characterized by scanning electron microscopy (SEM, Hitachi, S-4800H) and transmission electron microscopy (TEM, JEOL, JEM-2010F). Fourier transform-infrared spectroscopy (FT-IR) was carried out on a BRUKER EQUINOX55 instrument. X-ray photoelectron spectra (XPS) were measured on Thermo ESCALAB 250 Xi instrument.

Electrochemical measurements

Electrochemical performances of the Mn_3O_4 products were conducted using a three-electrode cell. The working electrode was prepared by mixing as-synthesized Mn_3O_4 with acetylene black and polytetrafluoroethylene at a weight ratio of 80 : 15 : 5 to form a homogeneous slurry. Then the slurry was pressed on the nickel foam current and dried at 60 °C for 12 h in a vacuum oven. The mixture pressed on the nickel foam was approximately 2.5 mg cm^{-2}. Pt electrode and saturated calomel electrode (SCE) electrode were regarded as the counter and reference electrodes, respectively. All electrochemical measurements were performed at room temperature using an electrochemical workstation (CHI660D Chenhua, China) in a conventional three-electrode cell in 1 M Na_2SO_4 solution. Cyclic voltammetry (CV) was carried out at different scan rates ranging from 5 to 50 mV s^{-1} in the potential window of −0.2 to 0.8 V. The galvanostatic charge–discharge (GCD) curves were measured at different current densities within the potential window between −0.2 and 0.8 V. Electrochemical impedance spectroscopy (EIS) was conducted at a frequency range of 10^5 to 10^{-2} Hz.

Results and discussion

Fig. 1a shows the schematic illustration of the formation of Mn_3O_4 hollow microcubes and solid nanospheres. The fabrication process was carried out through a two-step route.

In the first step, metal formate framework $[CH_3NH_3]$ $[Mn(HCOO)_3]$ templates were synthesized by a modified precipitation method.[34] Mn^{2+} reacted with formic acid neutralized by methylamine in ethanol solution at room temperature. The obtained precursors were characterized by XRD. As shown in Fig. 1b, all the diffraction peaks correspond to the simulated results, indicating they were single-phase products. The morphology of precursor was investigated by low-magnification SEM (Fig. 1c). The precursor had cubic shape and an average size of about 2 μm, and the surface was smooth.

In the next step, Mn_3O_4 was obtained by alkaline-solution treatment of the precursor under hydrothermal condition. According to the XRD results (Fig. 2), all the diffraction peaks can be well indexed to the tetragonal phase of Mn_3O_4 (space group $I4_1/amd$) with JCPDS card no. 01-1127, indicating high purity of the samples. Note that all the diffraction peaks of the products are significantly broaden in width and weaken in intensity, suggested that the as-obtained Mn_3O_4 are essentially
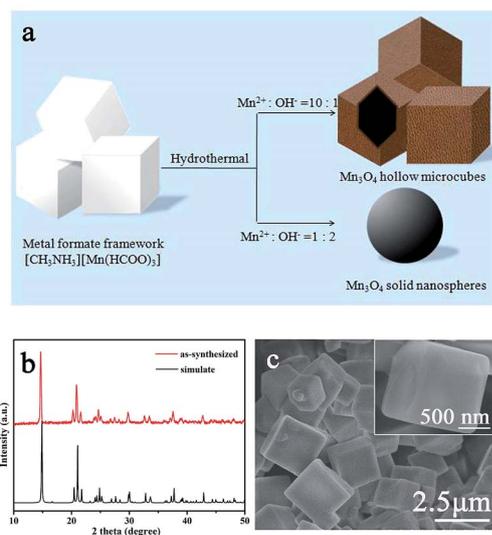
Fig. 1 (a) Schematic illustration of the formation of Mn_3O_4 hollow microcubes and solid nanospheres. XRD patterns (b) and SEM images (c) of precursor.

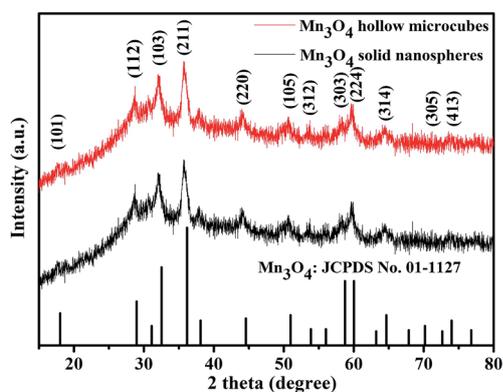Fig. 2 XRD patterns of Mn_3O_4 hollow microcubes and solid nanospheres.
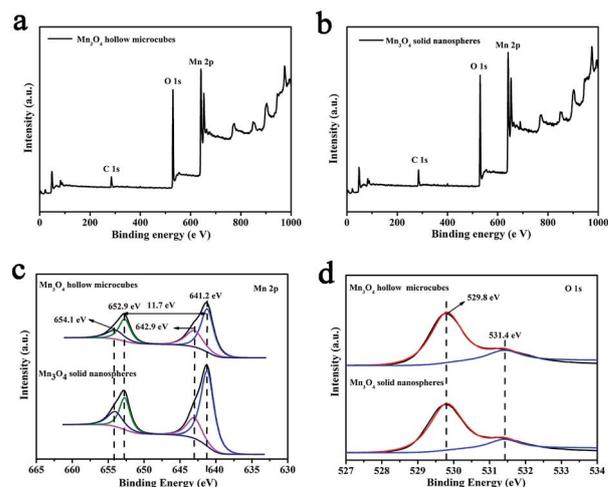

Fig. 3 XPS survey spectra for Mn_3O_4 hollow microcubes (a) and solid nanospheres (b); XPS spectra of Mn 2p (c) and O 1s (d).

constructed with nanosized primary crystallites. Additionally, the chemical compositions of the products were also analyzed by XPS. As shown in Fig. 3a and b, the main peaks located at 284.9, 530.1 and 641.0 correspond to C 1s, O 1s and Mn 2p, respectively. The Mn 2p spectra (Fig. 3c) were disassembled into four peaks: 641.2 and 654.1 eV corresponding to Mn^{2+}, while the peaks located at 642.9 and 652.9 eV corresponding to Mn^{3+}.[35] Particularly, the spin orbital separation between the binding energy peaks of Mn $2p_{1/2}$ and Mn $2p_{3/2}$ was 11.7 eV, which was in good agreement with those reported for Mn_3O_4.[36,37] Moreover, in the O 1s spectra (Fig. 3d), the binding energy located at 529.8 and 531.4 eV can be attributed to the lattice oxygen in Mn_3O_4 and H_2O, respectively.[36] Therefore, both XRD and XPS results verified successful synthesis of Mn_3O_4.

The morphologies and microstructures of the products were characterized by SEM and TEM. SEM images (Fig. 4a) show that Mn_3O_4 hollow microcubes inherit the cubic shape of precursor with the average size of about 2 μm. Moreover, inset of Fig. 4a

reveals the porous structure of hollow microcubes. TEM images (Fig. 4b and c) further confirm that Mn_3O_4 hollow microcubes are comprised of a large number of small nanoparticles. HRTEM image (Fig. 4d) shows that the d-spacing value is approximately 0.30 nm, corresponding to the (112) plane of Mn_3O_4.

In alkaline solution, the ion exchange reaction took place as described below: $[CH_3NH_3][Mn(HCOO)_3](s) + 2OH^-(aq) = Mn(OH)_2(s) + 3HCOO^-(aq) + CH_3NH_3^+(aq)$. With the reaction proceeding, OH^- ions continuously flowed inward and Mn^{2+} ions diffused outward to maintain this reaction. Then the precursor microcubes were gradually depleted, followed by growth of the $Mn(OH)_2$ shell. The ion exchange reaction was verified by FT-IR analyses (Fig. S1†). In the FT-IR spectrum of precursor, the dominant peaks located at 1350 and 1600 cm^{-1} were attributed to $HCOO^-$. The broad peaks located at 2865 and 3112 cm^{-1} were attributed to C–H and C–N stretching, respectively.[34] After NaOH treatment, the peaks of $HCOO^-$, C–H and
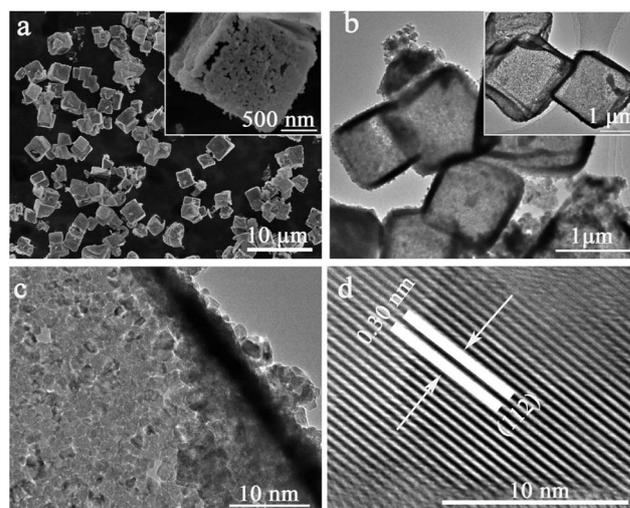

Fig. 4 SEM (a), TEM (b and c) and HRTEM (d) images of Mn_3O_4 hollow microcubes.

C–N were decreased obviously, while OH^- peak (3500 cm^{-1}) was appeared in the FI-TR spectrum of the product. The FT-IR spectra results evidenced the ion exchange reaction between $HCOO^-$ and OH^-. As $Mn(OH)_2$ can be easily oxidized by oxygen in autoclave during the hydrothermal process,[38–40] Mn_3O_4 was formed, and the formation process can be postulated below:

$$4Mn(OH)_2(s) + O_2(g) = 4MnOOH(s) + 2H_2O \quad (1)$$

$$2Mn(OH)_2(s) + 4MnOOH(s) = 2Mn_3O_4(s) + 4H_2O \quad (2)$$
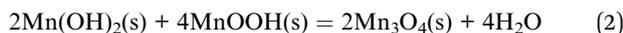
The effects of reaction conditions (reaction time and molar ratio) on the morphology of Mn_3O_4 were further investigated. When precursor $[CH_3NH_3][Mn(HCOO)_3]$ reacted with NaOH in a molar ratio of 10 : 1 and the reaction time was 6 h, OH^- ions were insufficient, and the ion exchange reaction was slow and incomplete. Finally, the residual precursors were dissolved in water, giving Mn_3O_4 hollow microcubes. When the molar ratio of $[CH_3NH_3][Mn(HCOO)_3]$ to NaOH was kept at 10 : 1 and the hydrothermal reaction time was prolonged to 12 h, the product was still pure Mn_3O_4 (Fig. S2†). However, Mn_3O_4 hollow micro-cubes were partly broken with the shell thickness increased (Fig. S3†). When the molar ratio was changed to 1 : 2 and the reaction time was 6 h, Mn_3O_4 nanoparticles were obtained (Fig. S4†). As the reaction time was then prolonged to 24 h, Mn_3O_4 solid nanospheres with larger sizes were generated instead. SEM image (Fig. 5a) shows that Mn_3O_4 solid nano-spheres are randomly arranged into a cluster with coarse surface, and the average diameter is about 300 nm. TEM images (Fig. 5b and c) display the solid nanospheres consist of numerous nanoparticles, evidencing the formation of Mn_3O_4 solid nano-spheres through the assembly of small nanoparticles. HRTEM image (Fig. 5d) presents that the lattice spacings are about 0.27 and 0.30 nm, which can be assigned to the (103) and (112) planes of Mn_3O_4 respectively.

Based on the above results, we propose the formation mechanism for the Mn_3O_4 hollow microcubes and solid nanospheres with secondary structures. As the alkaline solution is insufficient

firstly, $Mn(OH)_2$ nanoparticles are formed. When the concentration of OH^- ions is appropriate, OH^- ions continuously flow inward and Mn^{2+} ions diffuse outward, leading to the formation of well-distributed $Mn(OH)_2$ shell on the precursor surface. Finally, Mn_3O_4 hollow microcubes are obtained with the disso-lution of the residual precursors. When the concentration of OH^- ions is increased, the excess OH^- ions significantly accelerate the ion exchange reaction. The cubic structure is destroyed completely in the initial stage of the ion exchange reaction. Therefore, Mn_3O_4 nanoparticles and solid nanospheres are generated with the extension of the reaction time.

The electrochemical properties of Mn_3O_4 electrode materials were evaluated by CV, GCD and cycling stability in 1 M aqueous Na_2SO_4 solution. Fig. S5† shows the CV and GCD curves of Mn_3O_4 hollow microcubes and solid nanospheres at various scan rates (from 5 to 50 mV s^{-1}) and current densities (from 0.3 to 5 A g^{-1}). Fig. 6a shows the CV curves of Mn_3O_4 hollow microcubes and solid nanospheres electrodes at the scan rate of 10 mV s^{-1} in the potential window of −0.2 to 0.8 V vs. SCE. Each CV curve has almost rectangular shape and symmetry, indi-cating a typical pseudocapacitor feature. Fig. 6b gives the measured GCD curves of Mn_3O_4 hollow microcubes and solid nanospheres electrodes at the current density of 0.5 A g^{-1}. The specific capacitances can be calculated from the discharge curves according to the following equation:

$$C = I\Delta t/m\Delta V \quad (3)$$

where I is the discharge current density, m is the mass of active materials, Δt is the discharge time (s), and ΔV is the voltage window (V). As shown in Fig. 6c, the calculated specific capac-itances of Mn_3O_4 hollow microcubes and solid nanospheres are 176, 152, 124, 116, 105, 90 and 150, 131, 113, 108, 100, 85 F g^{-1} at the current densities of 0.3, 0.5, 1, 2, 3 and 5 A g^{-1}, respec-tively. With increasing current density from 0.3 to 5 A g^{-1}, 51%
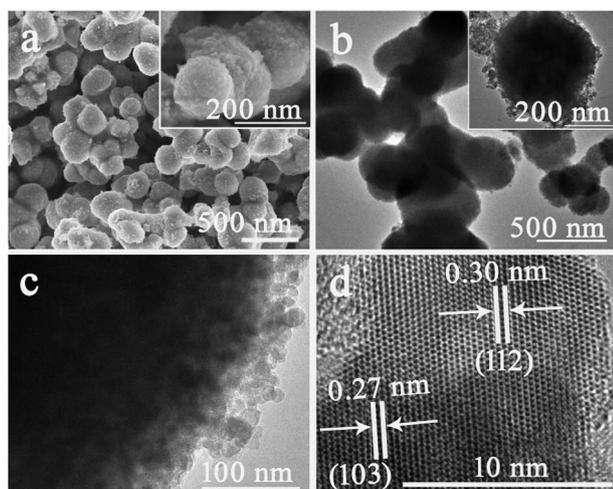

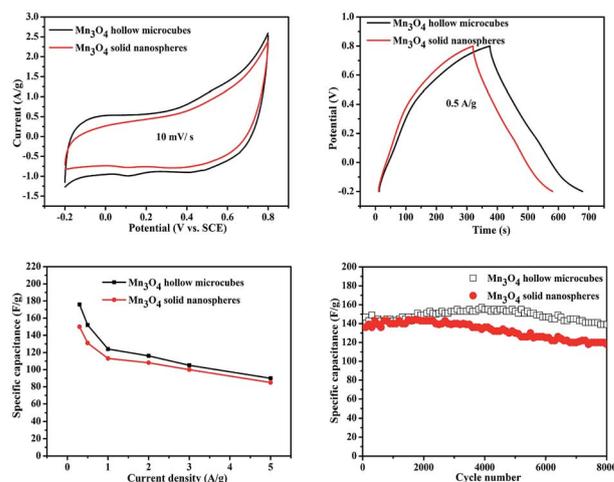Fig. 5 SEM (a), TEM (b and c) and HRTEM (d) images of Mn_3O_4 solid nanospheres.

Fig. 6 CV (a) and GCD (b) curves of Mn_3O_4 hollow microcubes and solid nanospheres. (c) Specific capacitances of Mn_3O_4 hollow micro-cubes and solid nanospheres at different current densities. (d) Cycling stability of Mn_3O_4 hollow microcubes and solid nanospheres at the current density of 2 A g^{-1}.
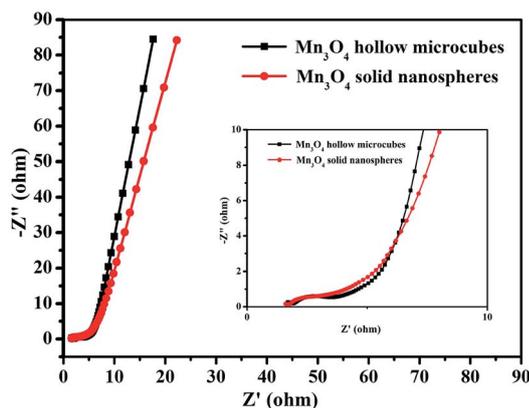
Fig. 7 EIS results of Mn_3O_4 hollow microcubes and solid nanospheres.

and 56% of the specific capacitances were retained respectively. Obviously, the specific capacitance of Mn_3O_4 hollow microcubes was higher than that of solid nanospheres, mainly because the formers had more active sites that facilitated the transport of electrons and electrolyte ions.

The long-term cycling stability of Mn_3O_4 hollow microcubes and solid nanospheres is shown in Fig. 6d. The specific capacitance of Mn_3O_4 solid nanospheres remained in the first 3000 cycles and decreased slightly over the next 5000 cycles. The specific capacitance of Mn_3O_4 hollow microcubes increased slightly in the first 5000 cycles and decreased slightly over the next 3000 cycles. The results can mainly be ascribed to the activation of electrode materials, as the electrolyte needed time to penetrate their inner space.[41]

EIS was performed to evaluate the electrochemical performances of the two Mn_3O_4 electrodes with different morphologies. As exhibited in Fig. 7, the two depressed semicircles in the high-frequency region correspond to the resistances of electrolyte. The resistances of Mn_3O_4 hollow microcubes and solid nanospheres were 1.43 and 1.76 Ω, respectively, revealing that the formers had higher electron transfer ability. A straight line in the low-frequency region represented the Warburg impedance, as the electrolyte diffusion into electrode materials. Since Mn_3O_4 hollow microcubes exhibit a more vertical line than Mn_3O_4 solid nanospheres do, the formers had lower diffusive resistance. In short, the better electrochemical performance of Mn_3O_4 hollow microcubes can be attributed to the more active sites and lower diffusive resistance. We compared the electrochemical performance of Mn_3O_4 hollow microcubes and solid nanospheres with the reported Mn_3O_4 based electrode materials especially taking into consideration the existence of additional carbon modifications, which are listed in Table S1.†[42–46] The comparison further suggests that the Mn_3O_4 hollow microcubes and solid nanospheres exhibit improved electrochemical performance with better capacitance and excellent cycling stability.

Conclusions

In summary, we reported a facile strategy to prepare two Mn_3O_4 products with different morphologies from an MOF template. When used as supercapacitor electrode materials, Mn_3O_4 hollow microcubes and solid nanospheres had high specific capacitances of 176 F g^{-1} and 150 F g^{-1} respectively at a current density of 0.3 A g^{-1}, and the specific capacitance retentions were 95% and 86% respectively after 8000 charge–discharge cycles at a current density of 2 A g^{-1}. Mn_3O_4 hollow microcubes had higher specific capacitance than that of Mn_3O_4 solid nanospheres, because the formers had more active sites and lower diffusive resistance. The fabricated Mn_3O_4 hollow microcubes and solid nanospheres are promising for supercapacitor applications.

Acknowledgements

Notes and references

1 J. R. Miller and P. Simon, *Science*, 2008, **321**, 651–652.
2 M. F. El-Kady, V. Strong, S. Dubin and R. B. Kaner, *Science*, 2012, **335**, 1326–1330.
3 P. Simon, Y. Gogotsi and B. Dunn, *Science*, 2014, **343**, 1210–1211.
4 X. Zhao, B. M. Sanchez, P. J. Dobson and P. S. Grant, *Nanoscale*, 2011, **3**, 839–855.
5 G. Wang, L. Zhang and J. Zhang, *Chem. Soc. Rev.*, 2012, **41**, 797–828.
6 Y. Huang, J. Liang and Y. Chen, *Small*, 2012, **8**, 1805–1834.
7 H. Jiang, P. S. Lee and C. Li, *Energy Environ. Sci.*, 2013, **6**, 41–53.
8 G. Salitra, A. Soffer, L. Eliad, Y. Cohen and D. Aurbach, *J. Electrochem. Soc.*, 2000, **147**, 2486–2493.
9 C. Vix-Guterl, E. Frackowiak, K. Jurewicz, M. Friebe, J. Parmentier and F. Béguin, *Carbon*, 2005, **43**, 1293–1302.
10 H. Ye, Y. Cheng, T. Hobson and L. Jie, *Nano Lett.*, 2010, **10**, 2727–2733.
11 Y. Wang, S. F. Yu, C. Y. Sun, T. J. Zhu and H. Y. Yang, *J. Mater. Chem.*, 2012, **22**, 17584–17588.
12 J. Chen, Y. Huang, C. Li, X. Chen and X. Zhang, *Appl. Surf. Sci.*, 2015, **360**, 534–539.
13 Y. G. Wang, Z. D. Wang and Y. Y. Xia, *Electrochim. Acta*, 2005, **50**, 5641–5646.
14 B. Vidyadharan, R. A. Aziz, I. I. Misnon, G. M. A. Kumar, J. Ismail, M. M. Yusoff and R. Jose, *J. Power Sources*, 2014, **270**, 526–535.
15 J. Ma, Q. Cheng, V. Pavlinek, P. Saha and C. Li, *New J. Chem.*, 2013, **37**, 722–728.
16 W. Wei, X. Cui, W. Chen and D. G. Ivey, *Chem. Soc. Rev.*, 2011, **40**, 1697–1721.
17 R. Zhang, T. Zhou, L. Wang, Z. Lou, J. Deng and T. Zhang, *New J. Chem.*, 2016, **40**, 6796–6802.
18 M. M. Titirici, A. Markus Antonietti and A. Thomas, *Chem. Mater.*, 2006, **18**, 3808–3812.

19 M. Agrawal, S. Gupta, A. Pich, N. E. Zafeiropoulos and M. Stamm, *Chem. Mater.*, 2009, **21**, 5343–5348.

20 L. Zhang and H. Wang, *ACS Nano*, 2011, **5**, 3257–3267.

21 M. Pang and H. C. Zeng, *Langmuir*, 2010, **26**, 5963–5970.

22 J. Gascon, A. Corma, F. Kapteijn and F. X. L. I. Xamena, *ACS Catal.*, 2013, **4**, 361–378.

23 P. Kaur, J. T. Hupp and S. B. T. Nguyen, *ACS Catal.*, 2011, **42**, 819–835.

24 J. K. Sun and Q. Xu, *Energy Environ. Sci.*, 2014, **7**, 2071–2100.

25 L. Li, X. Wang, J. Liang, Y. B. Huang, H. F. Li, Z. J. Lin and R. Cao, *ACS Appl. Mater. Interfaces*, 2016, **8**, 9777–9781.

26 S. Xiong, Y. He, R. Krishna, B. Chen and Z. Wang, *Cryst. Growth Des.*, 2013, **13**, 2670–2674.

27 Z. J. Zhang, Z. Z. Yao, S. C. Xiang and B. L. Chen, *Energy Environ. Sci.*, 2014, **7**, 2868–2899.

28 Z. J. Lin, Y. B. Huang, T. F. Liu, X. Y. Li and R. Cao, *Inorg. Chem.*, 2013, **52**, 3127–3132.

29 X. D. Xu, R. J. Cao, S. Jeong and J. Cho, *Nano Lett.*, 2012, **12**, 4988–4991.

30 R. R. Salunkhe, J. Tang, Y. Kamachi, T. Nakato, J. H. Kim and Y. Yamauchi, *ACS Nano*, 2015, **9**, 6288–6296.

31 L. Zhang, H. B. Wu, S. Madhavi, H. H. Hng and X. W. Lou, *J. Am. Chem. Soc.*, 2012, **134**, 17388–17391.

32 L. Zhang, H. B. Wu and X. W. Lou, *J. Am. Chem. Soc.*, 2013, **135**, 10664–10672.

33 J. Zhang, Z. Lyu, F. Zhang, L. Wang, P. Xiao, K. Yuan, M. Lai and W. Chen, *J. Mater. Chem. A*, 2016, **4**, 6350–6356.

34 Z. Wang, B. Zhang, T. Otsuka, H. Kobayashi and M. Kurmoo, *Dalton Trans.*, 2004, **15**, 2209–2216.

35 Y. Umezawa and C. N. Reilley, *Anal. Chem.*, 1978, **50**, 1290–1295.

36 Y. Qiao, Q. Sun, H. Cui, D. Wang, F. Yang and X. Wang, *RSC Adv.*, 2015, **5**, 31942–31946.

37 F. Davar, M. Salavati-Niasari, N. Mir, K. Saberyan, M. Monemzadeh and E. Ahmadi, *Polyhedron*, 2010, **29**, 1747–1753.

38 J. Zhang, Y. Luan, Z. L. Yu, L. Wang, L. Xu, K. Yuan, F. Pan, M. Lai, Z. Liu and W. Chen, *Nanoscale*, 2015, **7**, 14881–14888.

39 L. C. Dong, Y. B. Zhong, S. Zhe, T. Y. Zheng and H. Wang, *RSC Adv.*, 2016, **6**, 21037–21042.

40 L. Balan, C. M. Ghimbeu, L. Vidal and C. Vix-Guterl, *Green Chem.*, 2013, **15**, 2191–2199.

41 Y. Cao, F. Yuan, M. Yao, J. H. Bang and J. H. Lee, *CrystEngComm*, 2014, **16**, 826–833.

42 M. Fang, X. L. Tan, M. Liu, S. H. Kang, X. Y. Hu and L. D. Zhang, *CrystEngComm*, 2011, **13**, 4915–4920.

43 Z. X. Liu, Y. Xing, S. M. Fang, X. W. Qu, D. P. Wu, A. Q. Zhang and B. Xu, *RSC Adv.*, 2015, **5**, 54867–54872.

44 J. W. Lee, A. S. Hall, J. D. Kim and T. E. Mallouk, *Chem. Mater.*, 2012, **24**, 1158–1164.

45 K. B. Wang, X. B. Shi, A. M. Lu, X. Y. Ma, Z. Y. Zhang, Y. N. Lu and H. J. Wang, *Dalton Trans.*, 2014, **44**, 151–157.

46 J. Y. Qu, F. Gao, Q. Zhou, Z. Y. Wang, H. Han, B. B. Li, W. B. Wan, X. Z. Wang and J. S. Qiu, *Nanoscale*, 2013, **5**, 2999–3005.